Supplement of Atmos. Chem. Phys., 22, 14547–14570, 2022
https://doi.org/10.5194/acp-22-14547-2022-supplement

Atmospheric Chemistry and Physics
Open Access
EGU

Supplement of

Towards sector-based attribution using intra-city variations in satellite-based emission ratios between CO_2 and CO

Dien Wu et al.

Correspondence to: Dien Wu (dienwu@caltech.edu)

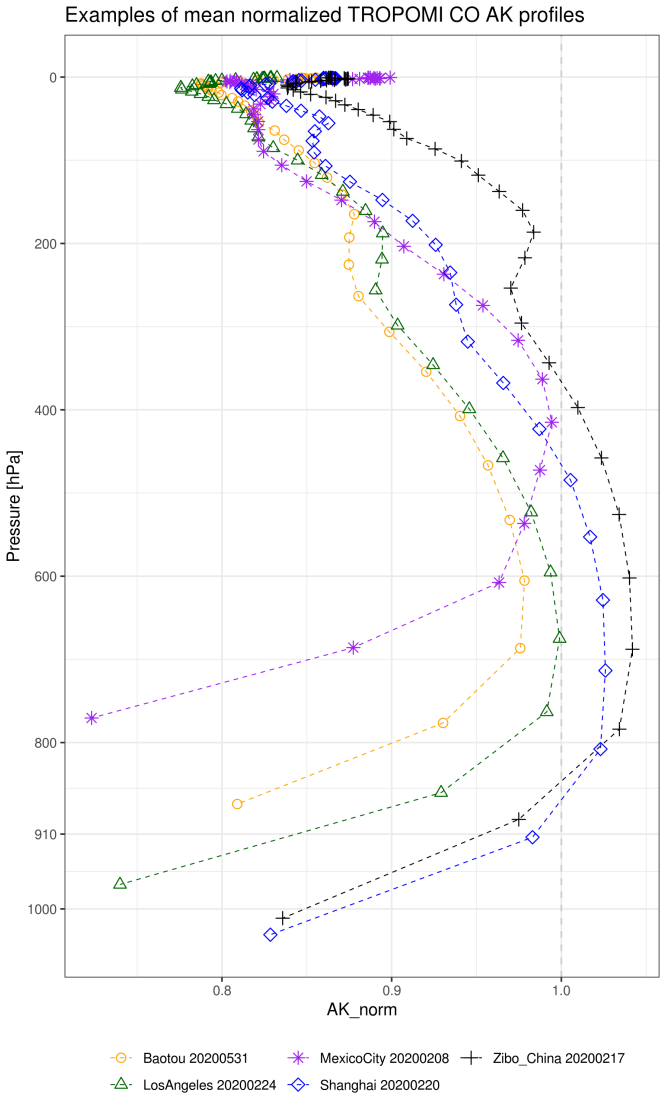

Figure S1. Examples of normalized averaging kernel [unitless] profiles from TROPOMI XCO, averaged over multiple soundings for one overpass per city. Colors denote the different overpasses. Normalized AKs are mostly lower than one for levels near the surface.

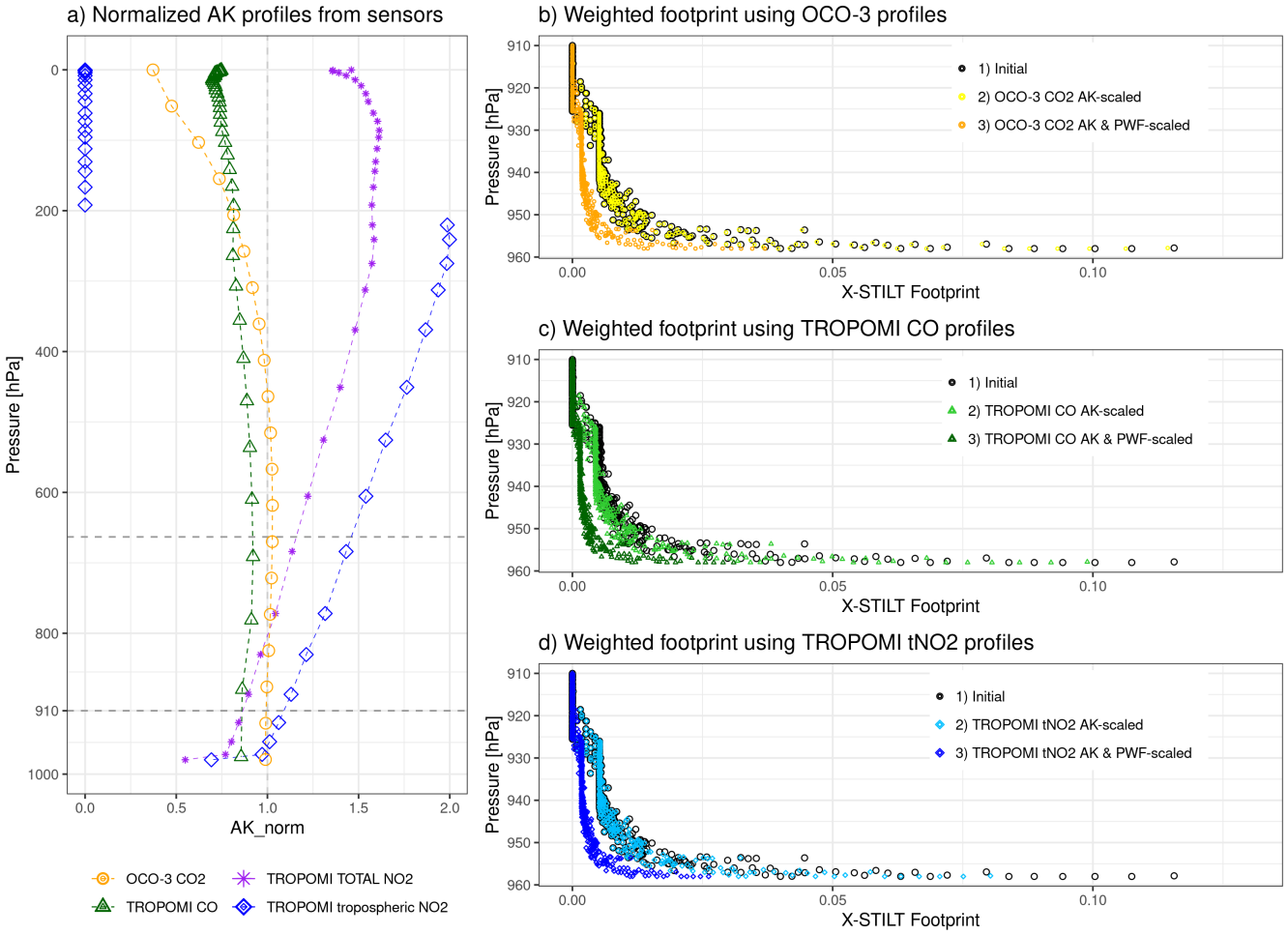

Figure S2. Demonstration of how AK and PWF are incorporated into the calculation of STILT footprint for every vertical level. (a) Example of normalized AK profiles from OCO-3 XCO_2, TROPOMI XCO and NO_2. For TROPOMI NO_2 AKs, profiles for both the total (purple stars) and tropospheric column (blue diamonds) are shown. (b-d) The vertical weighting procedure of the initial STILT footprint (black circles) using sensor-specific AKs (light yellow/green/blue circles) and using both AKs and pressure weighting functions (dark orange/green/blue circles). The footprint values are tied to every air parcel originating from the vertical column of the sounding. Footprints for air parcels at different altitudes will be weighted accordingly given the sensor-specific profiles. Note that this weighting procedure has now been implemented in X-STILT. Please refer to the data and code availability section in the main text for using the model.

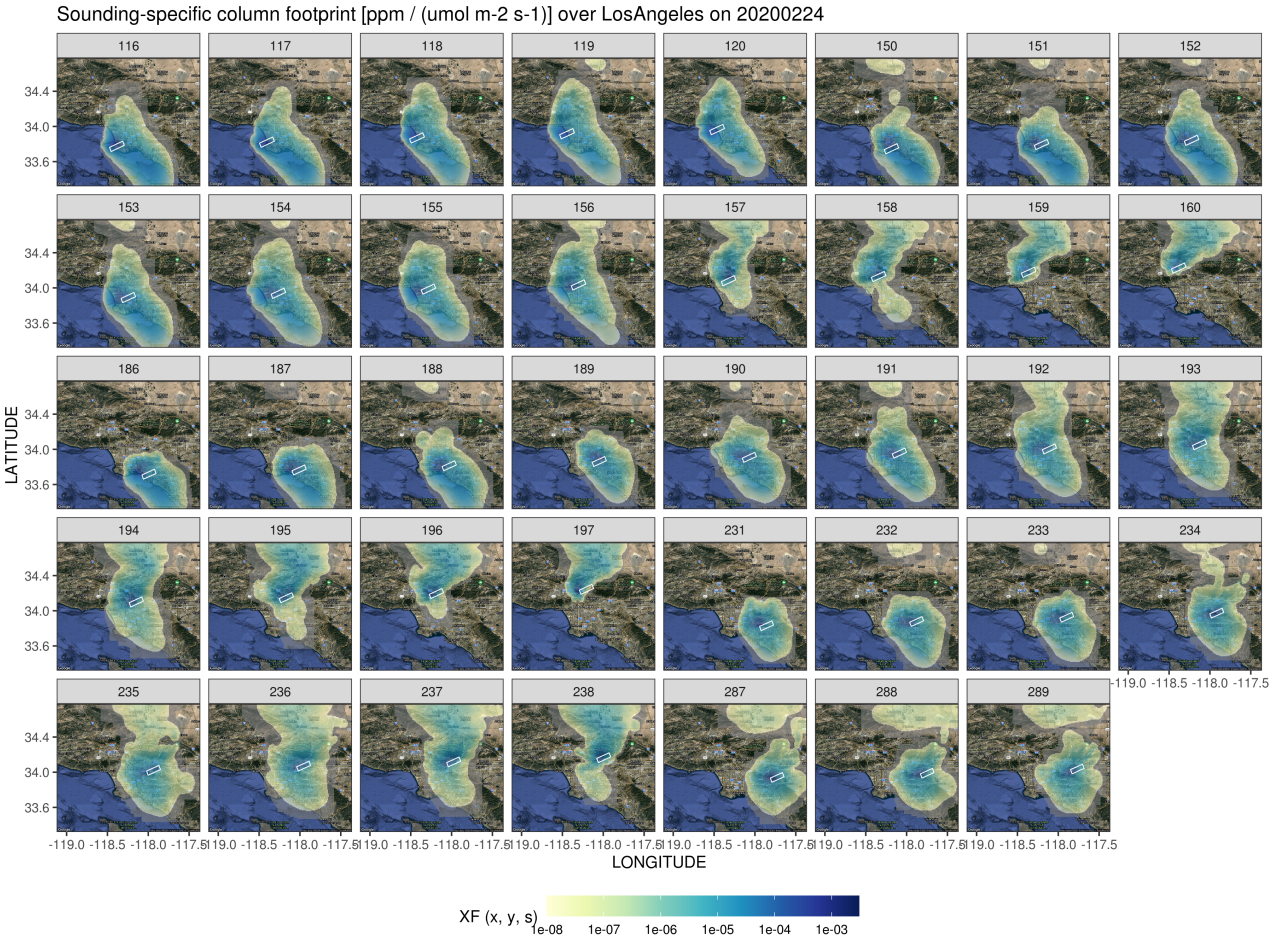

Figure S3. Spatial maps of column footprints $XF_{CO_2}(x, y, s)$ [ppm / (μmol m^{-2} s^{-1})] from X-STILT over LA on Feb 20, 2020. These column footprints are unique to each satellite sounding, given unique source-receptor relation. Note that the column footprint is initially generated for every OCO-2/3 sounding, but later aggregated to the TROPOMI scale (white rectangles). The column footprint for TROPOMI XCO can be slightly different from these maps due to discrepancies in AK profiles and atmospheric transport. The underlying hybrid maps were created using the ggmap library in R that adopted the Google Maps (copyright: Map data ©2021 Imagery ©2021 TerraMetrics).

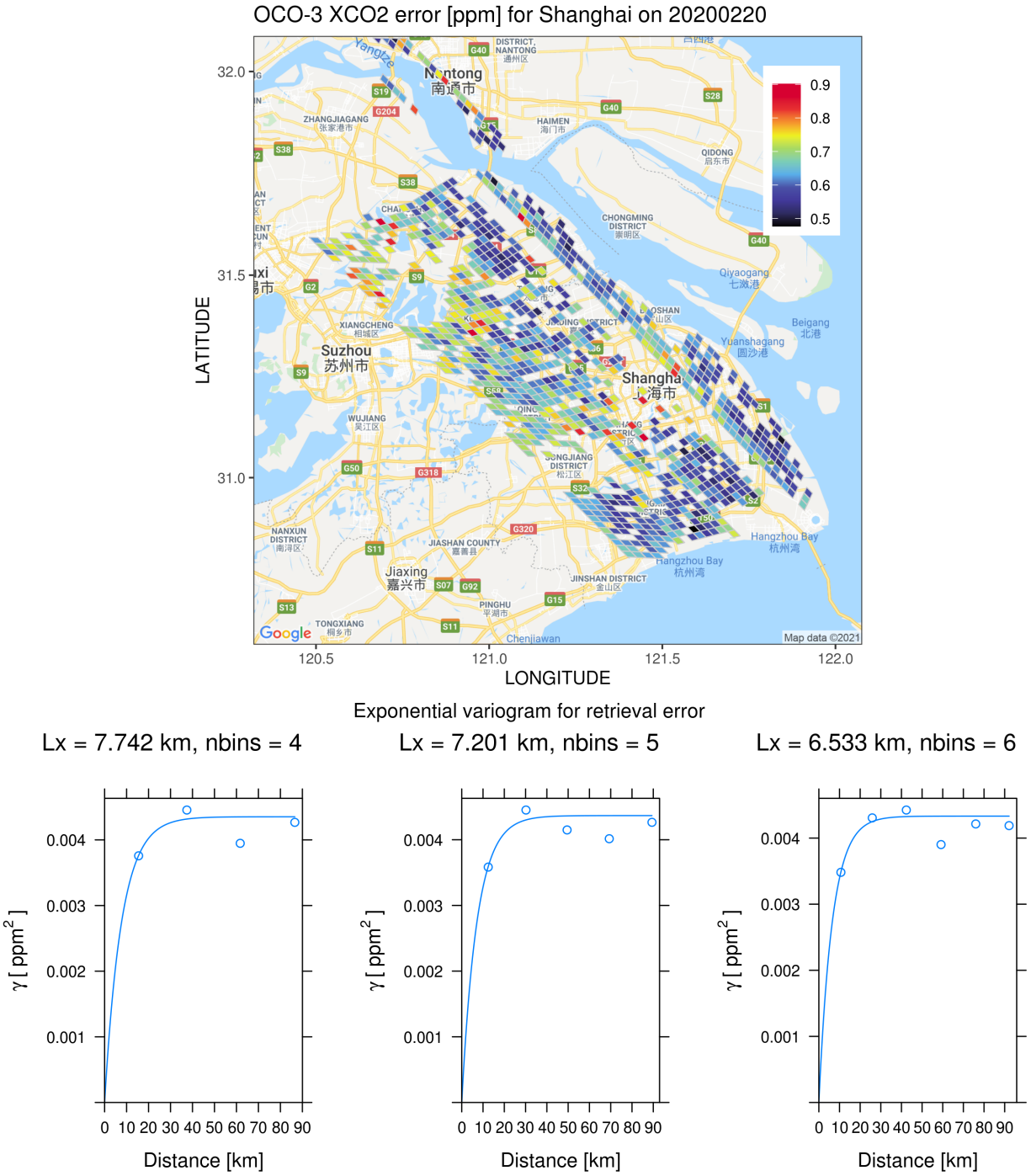

Figure S4. Upper Panel: An example of the sounding-specific XCO_2 retrieval errors from L2 files over Shanghai on Feb 20, 2020. **Lower Panels**: Exponential variogram analyses of retrieval errors and resultant error correlation length scale (L_x, km) with 4, 5, or 6 bins.

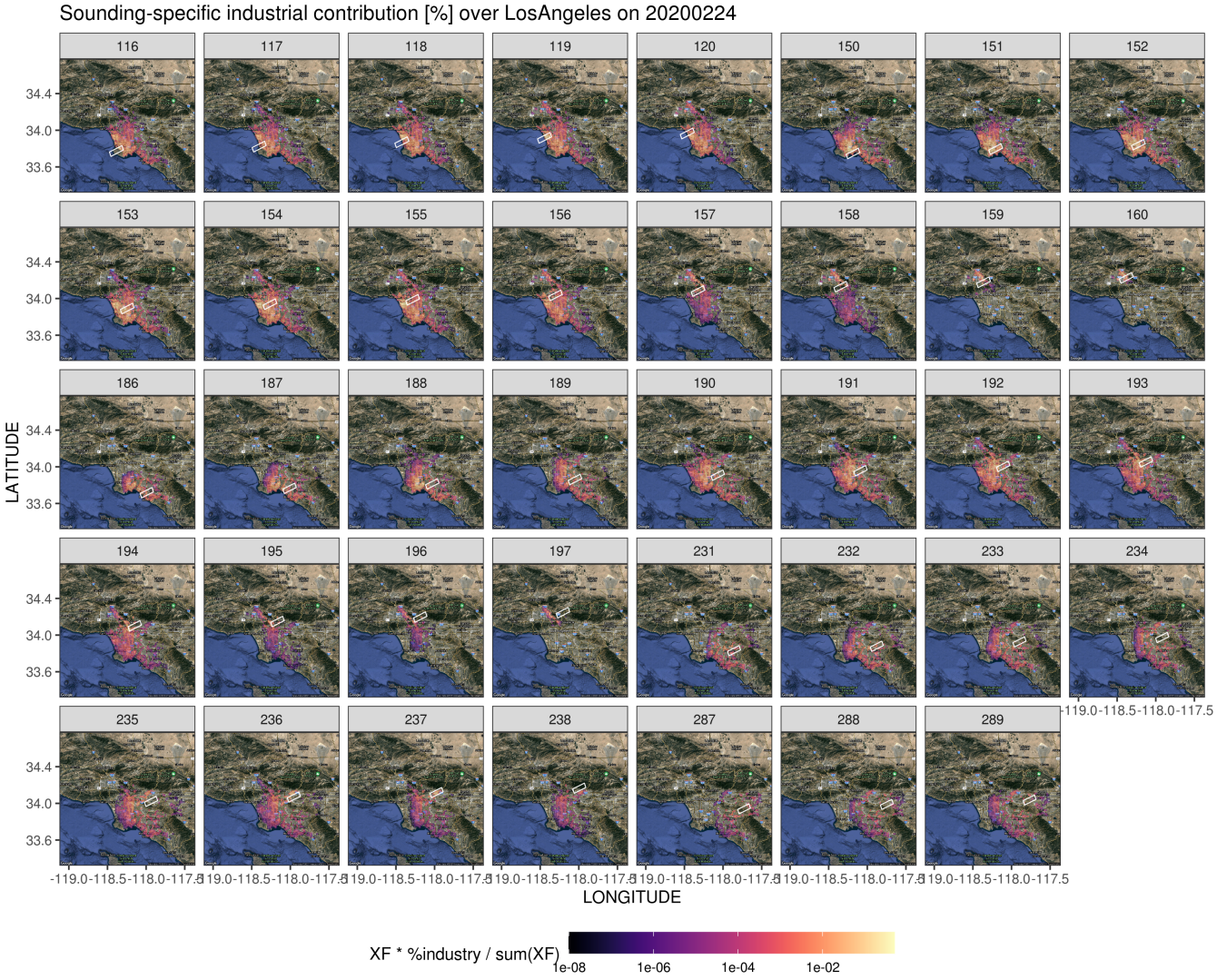

Figure S5. Spatial maps of the column footprint- normalized industry fraction ($P_{ind}(x, y)$ in %) over LA on Feb 20, 2020. Since the initial industry fraction from WUDAPT is normalized by the column footprint, these resultant normalized fractions $P_{ind}(x, y)$ show the influence of heavy industry on a given sounding (white rectangle). The lighter the color, the stronger impact from heavy industry. The underlying hybrid maps were created using the ggmap library in R that adopted Google Maps (copyright: Map data ©2021 Imagery ©2021 TerraMetrics).

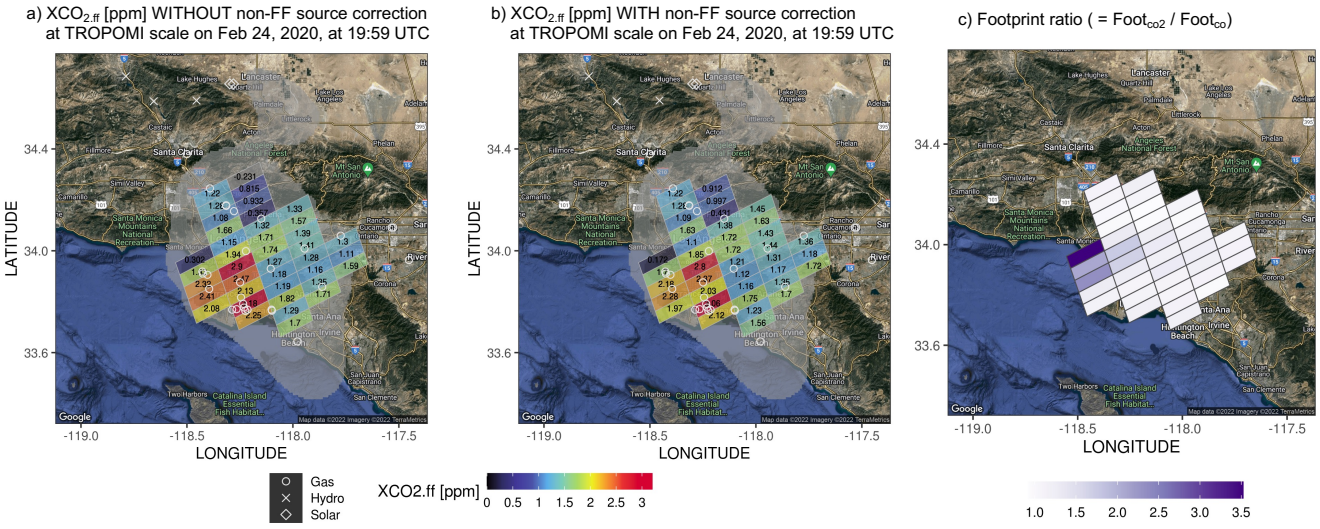

Figure S6. An example of the sounding-level information over LA on Feb 24, 2020. (a, b) XCO_2 FF enhancements BEFORE and AFTER correcting for the urban-background biogenic gradient. Since the biogenic gradient for the city center is usually positive, the XCO_2 enhancements with biogenic corrections shown in panel b are slightly smaller than those in panel a. (c) The ratio in the spatial sum of the column footprints between OCO-3 XCO_2 and TROPOMI XCO (i.e., $\gamma foot$ in **Eq. 2**). The two sets of footprints are different because of the difference in the AKs and wind fields. The higher the footprint ratio, the larger the discrepancy between the enhancement ratio and the emission ratio (**Eq. 2**). The underlying hybrid maps were created using the ggmap library in R that adopted Google Maps (copyright: Map data ©2021 Imagery ©2021 TerraMetrics).

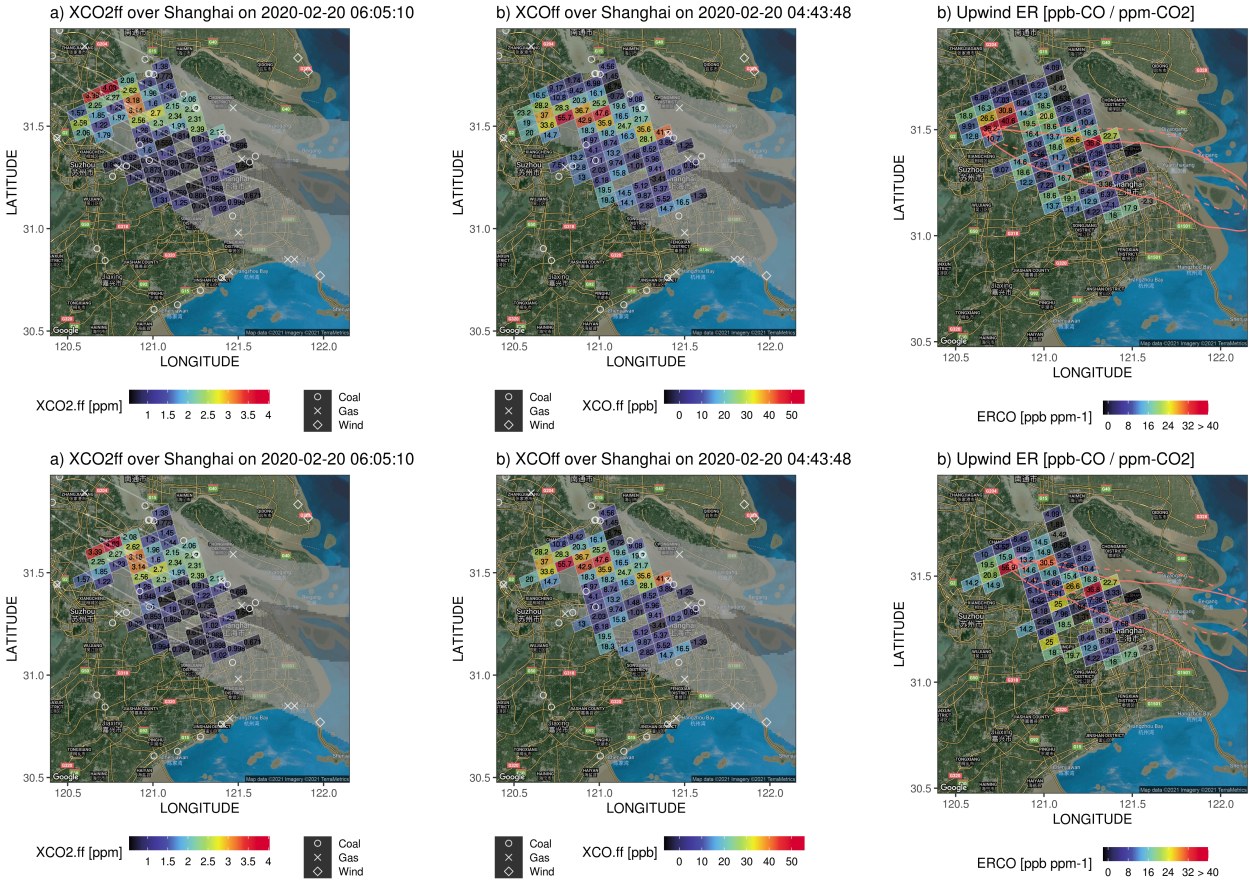

Figure S7. An example of XCO_2 and XCO FF enhancements over Shanghai on Feb 20, 2020. The first and the second row present the FF enhancements and sounding-level ER_{CO} before and after the plume shift, respectively. The gray regions indicate the source regions modeled by X-STILT. During the manual shifting procedure, XCO_2 enhancements move southward by 0 to 2 grids (depending on their longitudes) while XCO enhancements remain the same, leading to changes in the spatial distribution of ER_{CO} after re-aligning the urban plumes during the two overpass times. The correlation coefficient increases by 10% after the shift. The underlying hybrid maps were created using the ggmap library in R that adopted Google Maps (copyright: Map data ©2021 Imagery ©2021 TerraMetrics).

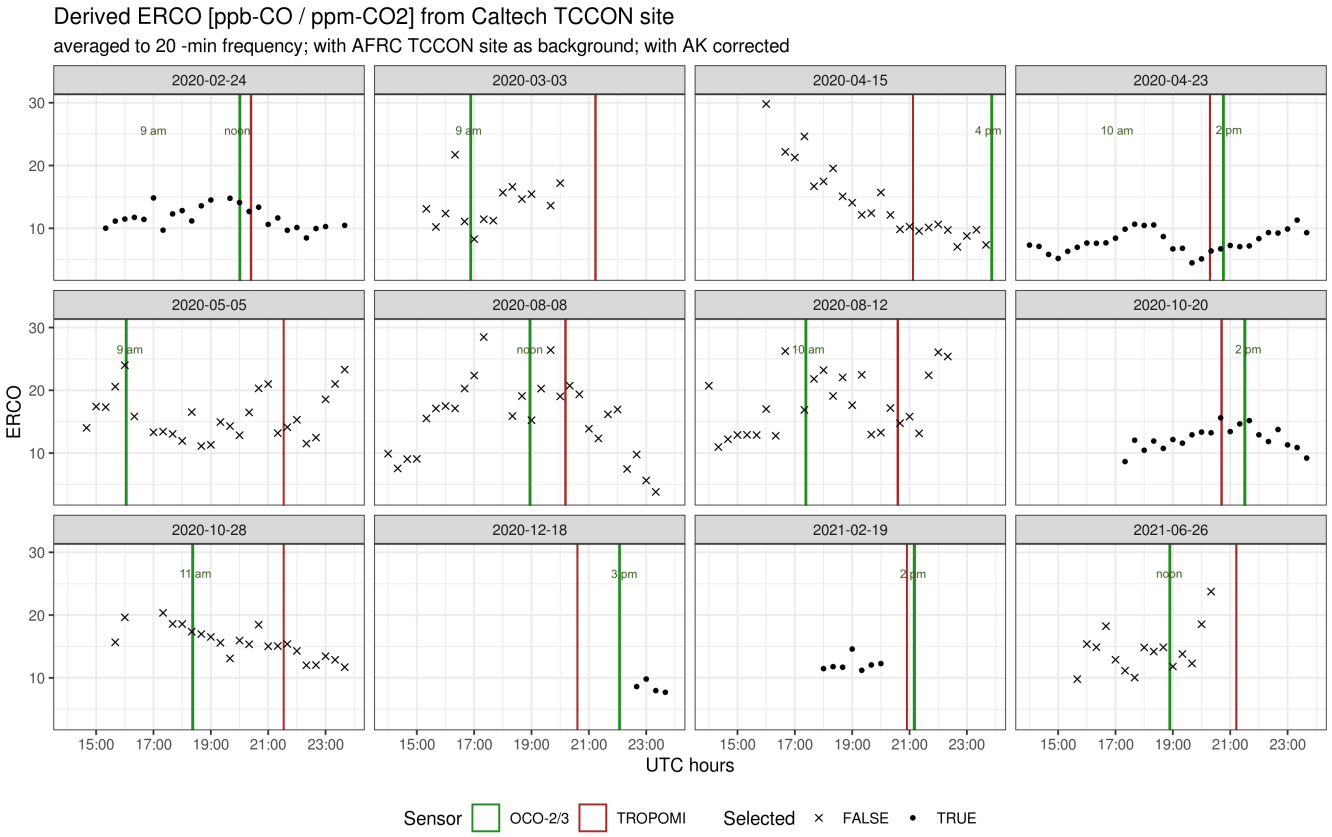

Figure S8. Time series of observed ERCO at the California Institute of Technology (Caltech) TCCON site (Wennberg et al., 2017) on the OCO-3 overpass dates till June 2021. The background is defined using the NASA Armstrong Flight Research Center (AFRC) site near Lancaster, California (Iraci et al., 2022). Column enhancements with corrections of TCCON averaging kernel are calculated following Hedelius et al. (2018). The overpasses that went into the final result are shown in solid black dots, while the remaining overpasses with significant plume shifts between OCO-3 and TROPOMI overpass times are shown in black crosses. The vertical lines indicate the OCO-3 (green) or TROPOMI (red) overpass times in UTC times. The day of the week for each date is shown as follows: Feb 24, 2020 (Mon), Mar 3 (Tues), Apr 15 (Wed), Apr 23 (Thurs), May 5 (Tues), Aug 8 (Sat), Aug 12 (Wed), Oct 20 (Tues), Oct 28 (Wed), Dec 18 (Fri), Feb 19, 2021 (Fri), and June 26, 2021 (Sat). Note that no qualified data exists during the overpass time of OCO-3 or TROPOMI on April 1, 2020. The TCCON data were obtained from the TCCON Data Archive hosted by CaltechDATA at https://tccondata.org. We thank Laura T. Iraci and Coleen M. Roehl for preparing the TCCON data for these two sites.

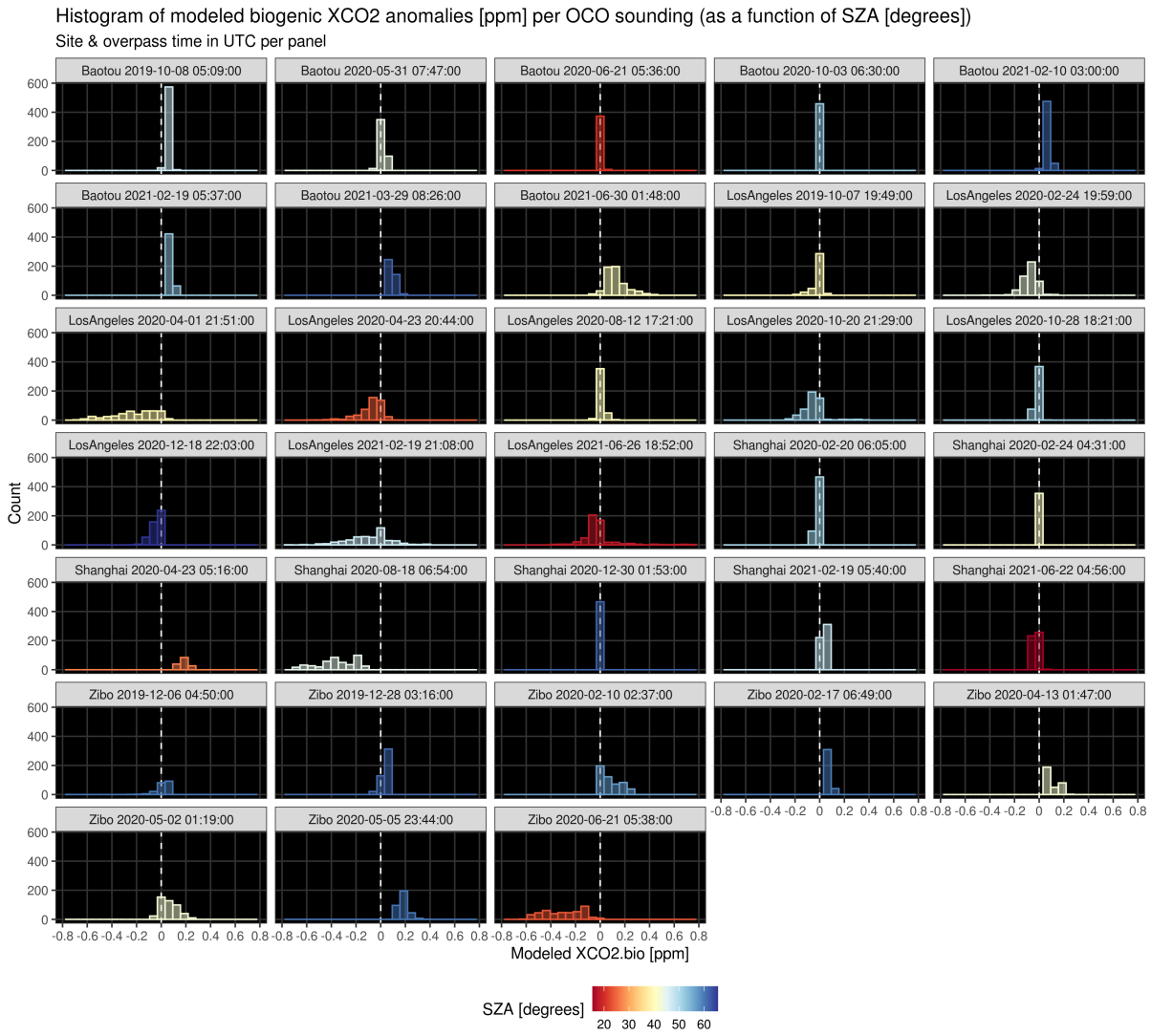

Figure S9. Histogram of modeled biogenic XCO_2 anomalies [ppm] at each OCO-2/3 sounding location with color code for different solar zenith angles (SZA) as an alternative way to indicate the overpass time. These biogenic anomalies are calculated as the spatial sum of the hourly column footprint and hourly NEE fluxes from a biospheric model. If the OCO-3 overpass time is close to noon (relative lower SZA), the daytime carbon sink dominates, leading to negative anomalies at the overpass time (e.g., dark green polygons in **Supplementary Fig. S10a,c**). In contrast, if the OCO-3 overpass time approaches morning or during the wintertime (relative higher SZA), the carbon uptake is weaker and the respiration dominates the biogenic fluxes, leading to net positive anomalies. Biogenic signals for Baotou and Shanghai are smaller compared to those for LA and Zibo. Note that these biogenic anomalies at the OCO scale were further averaged to the TROPOMI scale for calculating the observed urban XCO_2 signals. Also, not all overpasses shown here went into the final ER calculations, since some have substantial overpass time differences (**Fig. 8**). We stress again that the urban-background contrast of these anomalies (e.g., brown colors in **Supplementary Fig. S10b,d**) modify the anthropogenic enhancements, not the anomalies themselves. Please also refer to **Supplementary Fig. S10** that illustrates the modeled biogenic anomalies and their urban-background gradient for the two overpasses with the strongest biogenic influences.

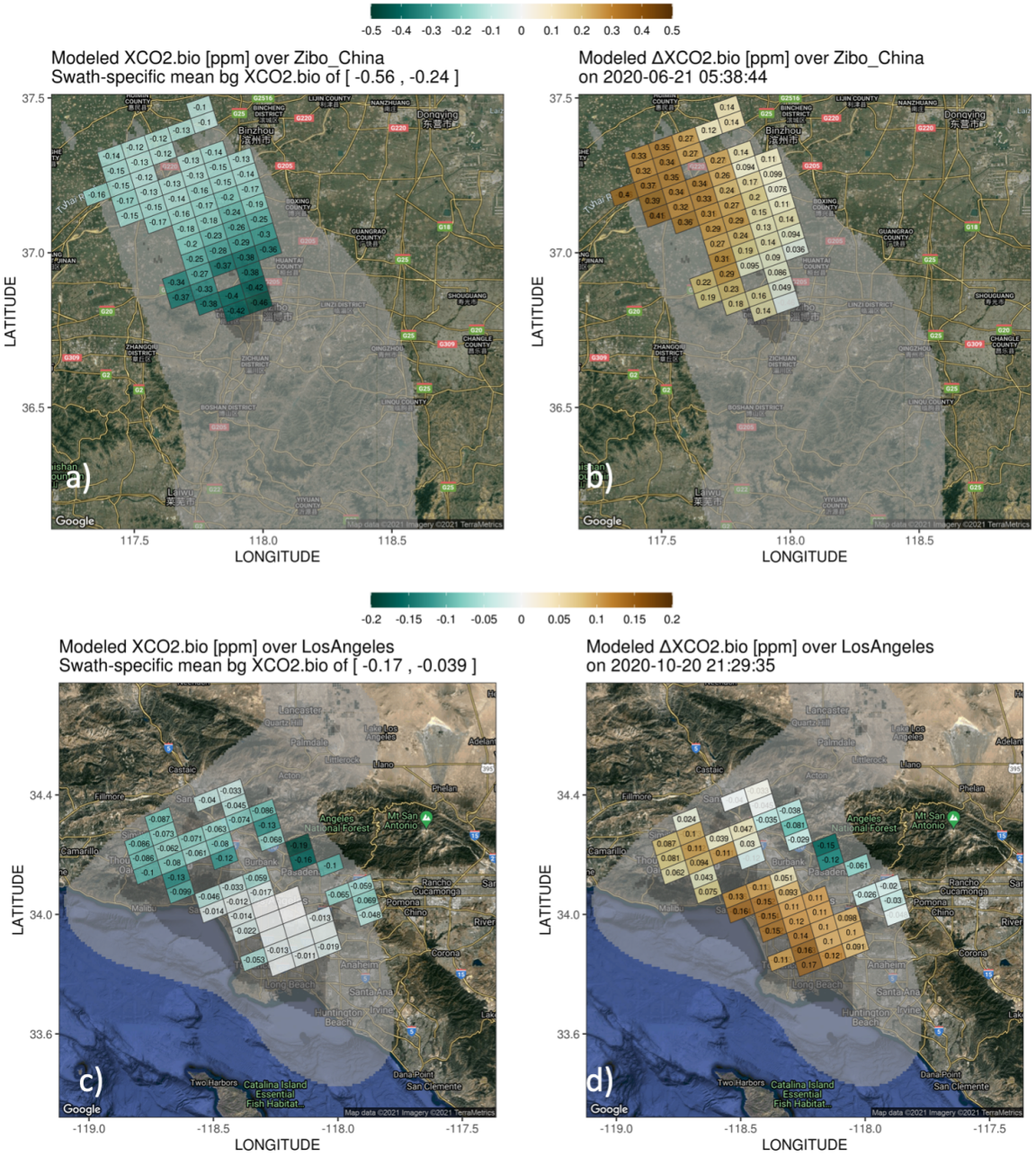

Figure S10. Spatial maps of modeled biogenic anomalies (a, c) and urban-background contrast (b, d) tied to each downwind satellite sounding for Zibo on June 21, 2020, and LA on Oct 20, 2020. For example, we chose the northern land outside the LA basin as the background. The background biogenic contribution is more negative than those biogenic anomalies in the basin. As a result, the gradient (δX_{bio}) for soundings in the basin now becomes positive. The underlying hybrid maps were created using the ggmap library in R that adopted Google Maps (copyright: Map data ©2021 Imagery ©2021 TerraMetrics).

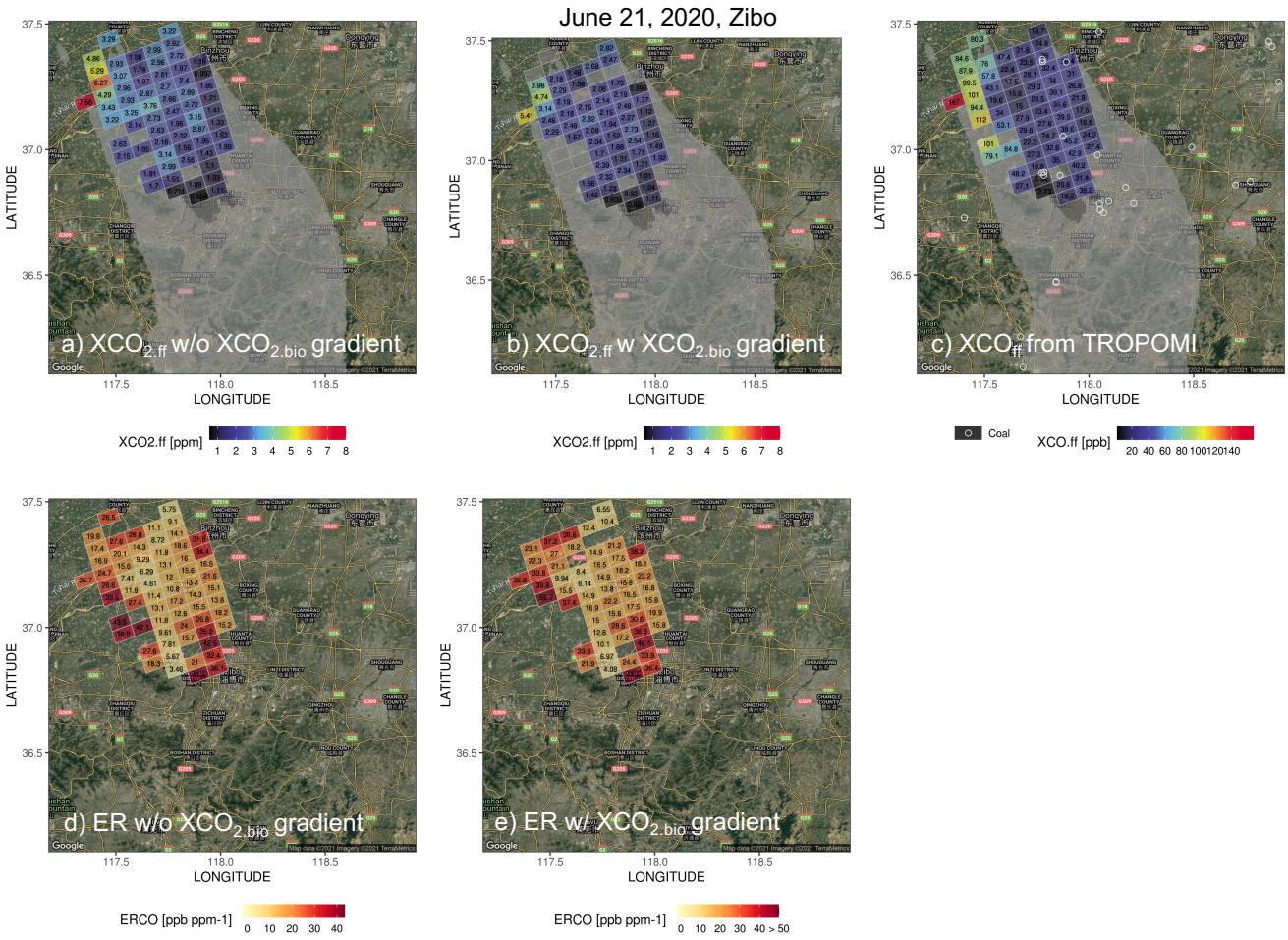

Figure S11. Spatial maps of derived FF enhancements (ppm-CO_2 in a, b and ppb-CO in c) and ER_{CO} (ppb ppm^{-1} in d, e) over Zibo on June 21, 2020, with and without taking the urban-rural biogenic gradient into account. Only soundings within the urban plume are displayed. The light grey shading denotes the near-field source region (defined by the X-STILT column footprint) with respect to those displayed soundings, given wind coming from the south. Considering the wind direction, observations further south of the displayed soundings are regarded as the background region (with latitude $< 36.8°$N, not plotted). As shown in **Fig. S10**, the biogenic gradient for soundings within the plume is normally positive. Such positive gradients are subtracted from the XCO_2 observations, leading to lower $FFCO_2$ signals (panel b versus a) and a higher ER_{CO} (panel e versus d) when correcting for the biogenic impact. The underlying hybrid maps were created using the ggmap library in R that adopted Google Maps (copyright: Map data ©2021 Imagery ©2021 TerraMetrics).

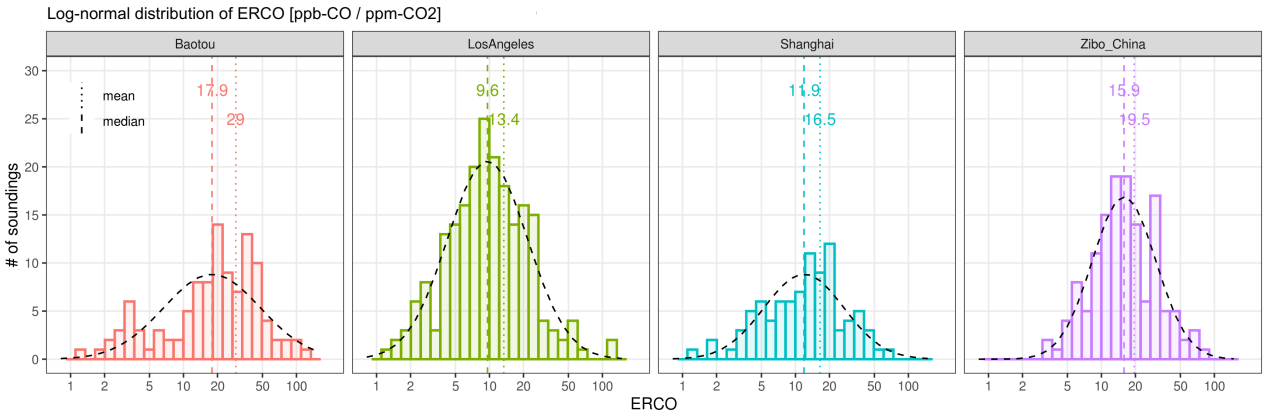

Figure S12. Distribution of ERs across four cities with the x-axis displayed in natural logarithm scale. The log-normal curve is shown as dashed lines. The estimated median/mean values of ERs based on a log-normal fit are shown as dashed/dotted vertical lines.

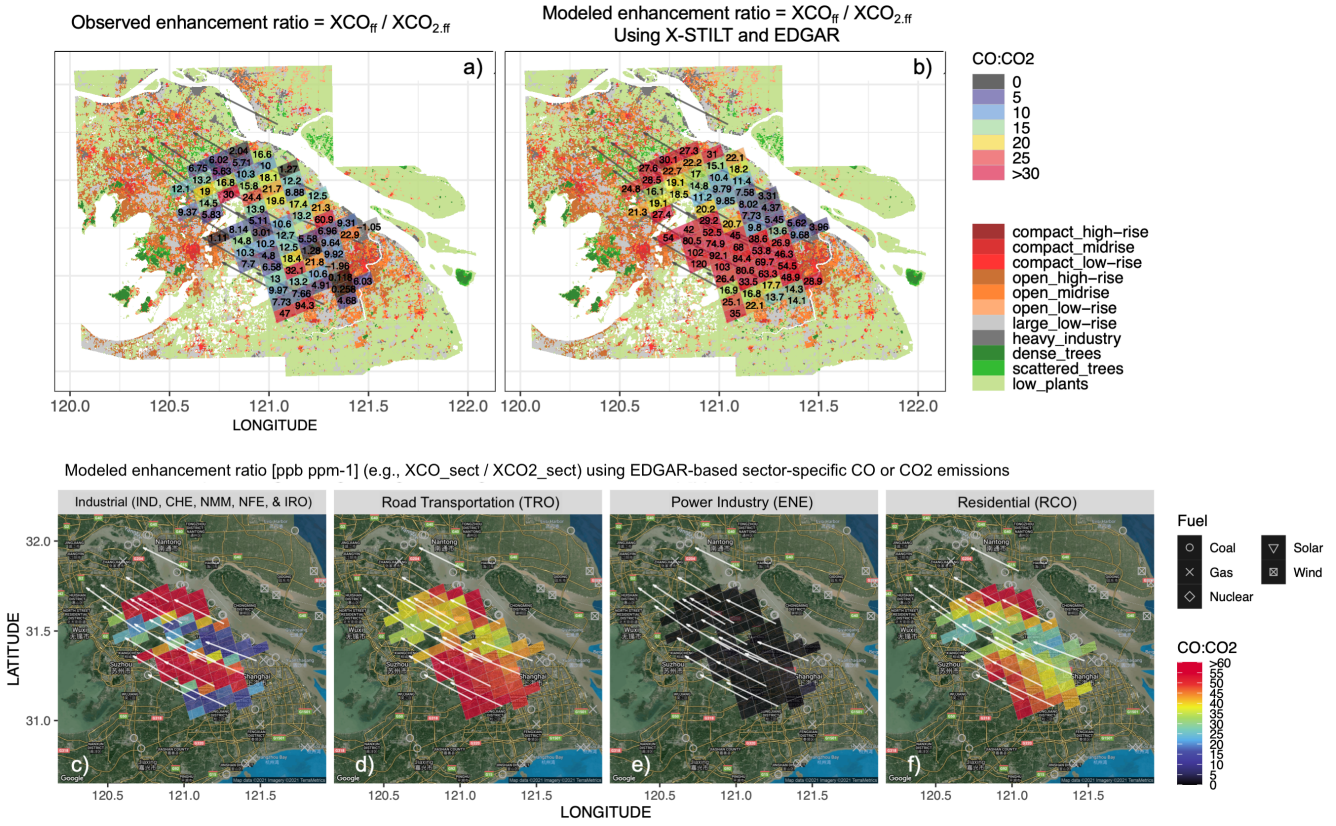

Figure S13. An example of the total FF enhancement ratios [ppb-CO / ppm-CO_2] observed from OCO-3 and TROPOMI (a) and simulated using X-STILT and EDGARv5 (b) over Shanghai on Feb 20, 2020. Maps of the simulated sectoral enhancement ratios [ppb-CO / ppm-CO_2] using sectoral emissions from EDGARv5 and X-STILT. Power plant locations from the global power plant dataset are displayed in various symbols with circles indicating the coal-fired power plants. Note that the underlying hybrid maps in the lower panels were created using the ggmap library in R that adopted Google Maps (copyright: Map data ©2021 Imagery ©2021 TerraMetrics).

References

Hedelius, J. K., Liu, J., Oda, T., Maksyutov, S., Roehl, C. M., Iraci, L. T., Podolske, J. R., Hillyard, P. W., Liang, J., Gurney, K. R., Wunch, D., and Wennberg, P. O.: Southern California megacity CO_2 , CH_4 , and CO flux estimates using ground-and space-based remote sensing and a Lagrangian model, Atmospheric Chemistry and Physics, 18, 16 271–16 291, https://doi.org/10.5194/acp-18-16271-2018, 2018.

Iraci, L., Podolske, J., Roehl, C., Wennberg, P. O., Blavier, J.-F., Allen, N., Wunch, D., and Osterman, G.: TCCON data from Armstrong Flight Research Center, Edwards (US), Release GGG2020R0, TCCON data archive, hosted by CaltechDATA, https://doi.org/10.14291/tccon.ggg2020.edwards01.R0, 2022.

Wennberg, P. O., Wunch, D., Roehl, C., Blavier, J.-F., Toon, G. C., and Allen, N.: TCCON data from Caltech (US), Release GGG2020R0, TCCON data archive, hosted by CaltechDATA, https://doi.org/10.14291/tccon.ggg2020.pasadena01.R0, 2017.